

Instrument Science Report WFC3 2008-40

WFC3 UVIS PSF Evaluation in Thermal-Vacuum Test #3

G. F. Hartig
20 August 2008

ABSTRACT

We have assessed the image quality of the WFC3 UVIS channel in a flight-like thermal-vacuum environment, and with its flight detector installed. Point source measurements at 16 field positions and four wavelengths indicate excellent imaging performance for the UVIS channel. Encircled energies readily meet expectations over the field, with CASTLE stimulus illumination. Models including the mid-frequency WFE of the HST OTA indicate that the on-orbit EE will likely meet the goal levels at 633 nm and meet the revised core CEI specification at 250 nm.

Introduction

We have previously discussed measurements of the UVIS PSF over the field, through four filters spanning the spectral range, in thermal-vacuum test #1, but with the detector not in its final flight configuration (Hartig 2005). The image quality was generally found to be excellent, but the detector has since been rebuilt, with a new TEC, and realigned. With the instrument in its final flight configuration we have made new image quality measurements with the CASTLE stimulus in the GSFC SES chamber during the thermal-vacuum #3 test (TV3), in Mar-Apr '08. The alignment of the detector within WFC3 and of the UVIS channel with respect to the CASTLE stimulus was determined to be nearly optimal during the TV3 test (Hartig 2008a) and the UVIS channel optical performance over the field, as assessed with wavefront error measurements is excellent (Hartig, 2008b).

Procedure

The PSF data were obtained in two epochs, as shown in Table 1. The measurements at 250 and 633 nm were obtained in the "cold operate" environment, while those at 350 and 810 nm were obtained at "hot operate". To maximize efficiency, 200 px square subarrays, approximately centered on each of the PSFs, were used to obtain pairs of images, through each of four filters: F275W, F336W, F625W and F814W, along with bias frames. The CASTLE provided narrow-band point source illumination with a 5 μ m pinhole, D2 lamp, and double monochromator with 13 nm bandpass, for the UV observations at 250 and 350

nm, and lasers at 633 and 810 nm through single-mode fibers for the R and I band filter data. The detector was operated at the nominal -83°C on-orbit temperature.

Table 1. TV3 PSF Observation Log

$\lambda(\text{nm})$	Filter	SMS	Date	Log	DB ID	Exp. (s)
250	F275W	UV11S01C	14-Mar-08	2008074c	51732:51792	20
350	F336W	UV11S02D	4-Apr-08	2008095a	55959:56019	2.5
633	F625W	UV11S03C	14-Mar-08	2008074c	51671:51731	1
810	F814W	UV11S04D	4-Apr-08	2008095a	56020:56080	1

In addition to the subarray images, pairs of deep full frame images, with the image cores saturated by factors of ~ 5 and 50, were also obtained at one field point for each of the 4 wavelengths, to better assess the PSF far wings and search for straylight effects, such as the CCD scatter halo seen at long wavelengths in the STIS and ACS HRC detectors. Dark images, following highly saturated PSF images, were also obtained to evaluate image persistence effects in the CCDs. As in the previous ambient testing (Hartig and Baggett, 2004b), no significant image persistence was discovered.

Analysis of the image pairs obtained for each wavelength/field point evinced a peculiarity that resulted in considerable follow-up testing: the second image of the pairs was almost invariably “sharper”, having a higher peak fraction and narrower width than the first image. The effect is strongest at the short exposures and very weak at the 20 s exposures used for the PSFs obtained at 250 nm. This was traced to vibration, induced by the UVIS shutter mechanism, of the optical train; most likely contributors are the POM and the M1 (corrector mechanism mirror), which have similar sensitivities. The PSF characteristics reported herein refer to the sharper images of the pairs that are less affected by this vibration, since on-orbit science observations will almost always use exposure times at which the vibration effect is expected to be small or entirely negligible; nevertheless, since they were obtained with exposures as short as 1 sec, there is certainly some degradation from the shutter vibration even in these images.

Results

A montage of the images at each field point is displayed for each wavelength, with a log stretch over ~ 6 dex, in Figure 1. The images are magnified by a factor 8 relative to the field size, and are located at the correct relative field positions. The diffraction-induced growth of the PSF with wavelength is readily apparent. Field-position dependent “donut” ghosts easily seen in the 250 nm, F275W images from TV1 (Hartig, 2005) are absent, as this filter was replaced in the interim (Brown, 2007). The images are well centered with respect to the format and no rotation is apparent, indicating excellent detector alignment.

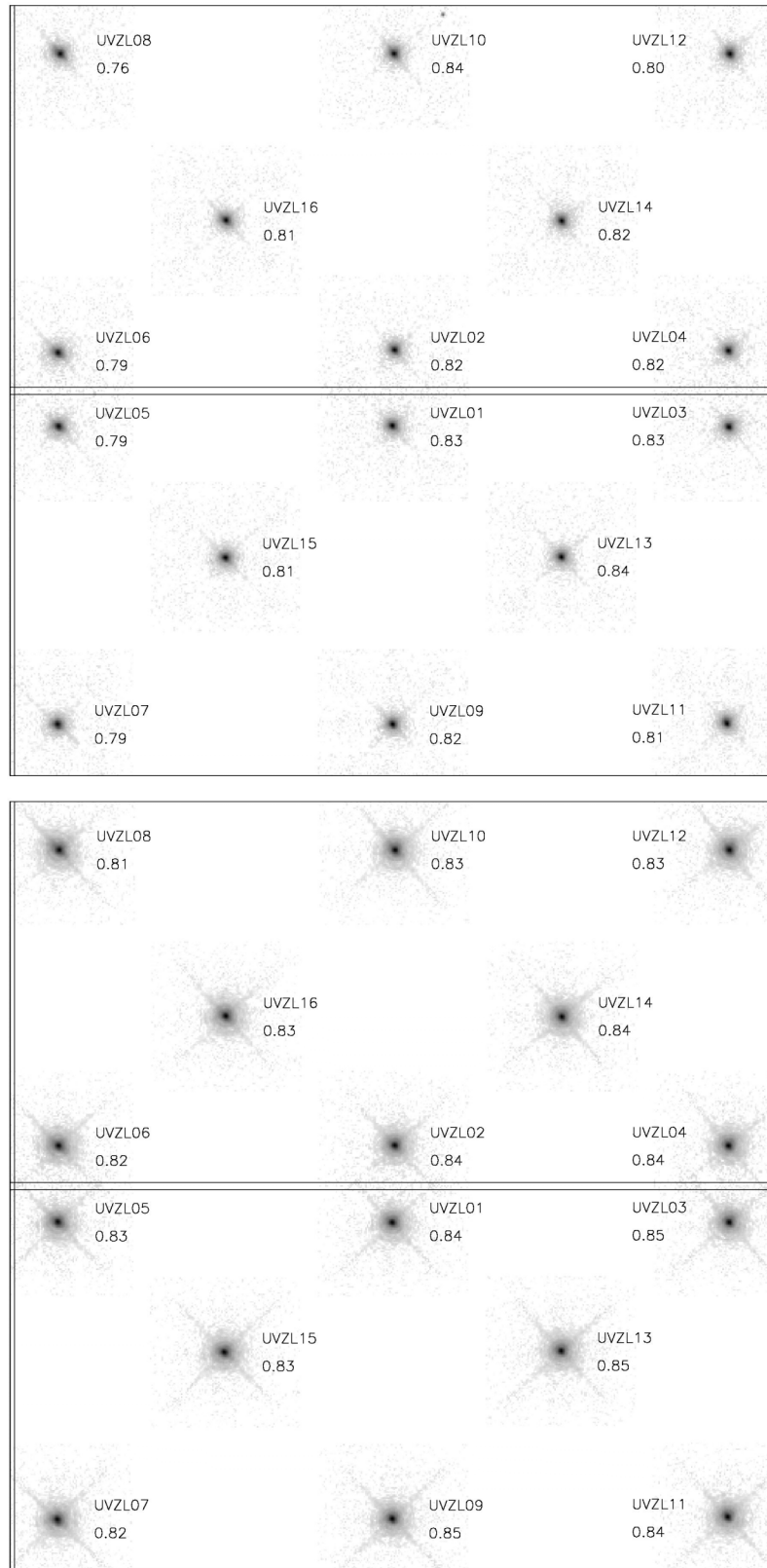


Figure 1. Montages of measured PSF images at 16 field points and at wavelengths 250 nm (top) and 350 nm (bottom). The images, shown centered at their actual locations in the field of view but with magnification of 8, have had background subtracted and first-order geometrical distortion removed. Measured encircled energy within diameters of 0.20 arcsec (250 nm) or 0.25 arcsec (all other wavelengths) are shown.

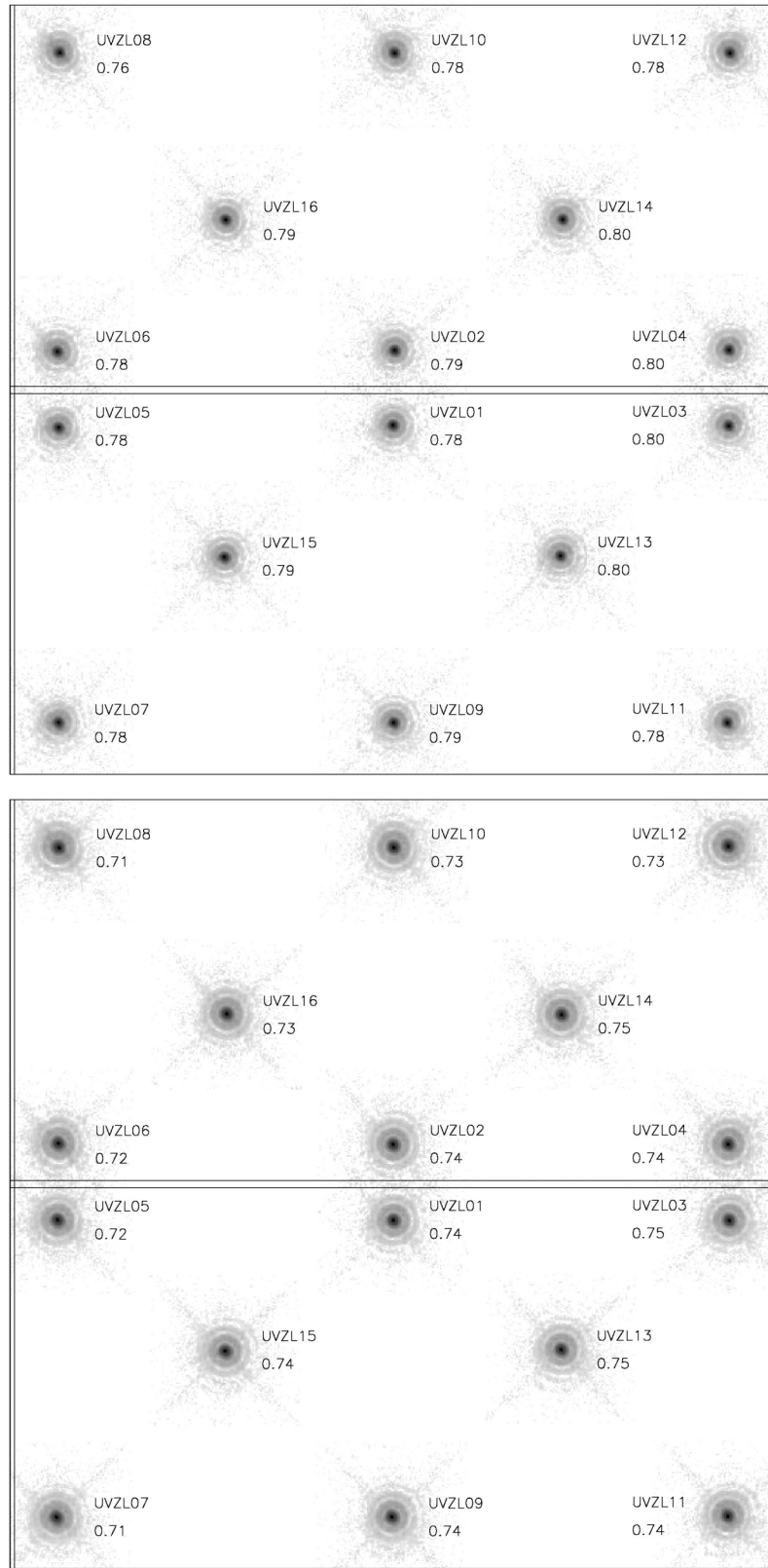


Figure 1 (cont'd). Montages of measured PSF images at 16 field points and at wavelengths 633nm (top) and 810 nm (bottom), indicating encircled energies within 0.25 arcsec diameter.

The encircled energy (EE) as function of radius from PSF center was computed for each of the unsaturated images, using IDL code previously developed and used for COSTAR, STIS and ACS alignment and verification. Briefly, the code corrects for first-order geometrical distortion, finds the image center at which the EE in a small diameter (0.15 arcsec) is maximized, computes the radius of each pixel from that center and, after subtracting a background that is adjusted so that the EE curve asymptotes to 1 with 0 gradient at a specified radius (2 arcsec for these subarray images), sums the normalized flux contribution within discrete radii, including estimation of partial pixel contributions. Table 2 presents the EE, in diameters from 0.15 to 0.35 arcsec, averaged over the field; the results for each of the measured field points are presented in Table 3, and shown in Figure 1 for diameters of 0.2 arcsec (250 nm) or 0.25 arcsec (other wavelengths). The peak pixel fraction (useful for exposure time estimation with regard to saturation avoidance), image width in pixels and sharpness parameter (sum of unity-sum-normalized PSF) are also included in Tables 2 and 3. Note that the peak fraction is highly sensitive to centration on the pixel grid, especially at short wavelengths where the Airy disk is undersampled. Previous modeling has shown that PSFs centered on the pixel corners can produce peak fraction ~5% (absolute) lower than those centered on a pixel, at 250 nm (Hartig and Baggett, 2004a). The peak fraction, width and sharpness are all sensitive to the shutter vibration effect, so their values in Table 2 are probably not representative of typical (longer) science exposures, since they were obtained with short exposure times.

Table 2. Mean Measured Encircled Energy and Other PSF Parameters

PSF Parameter Average Over Field							
λ (nm)	peak	0.15	0.20	0.25	0.35	FWHM (px)	sharp
250	0.156	0.702	0.811	0.867	0.918	1.925	0.069
350	0.136	0.657	0.775	0.835	0.895	2.081	0.057
633	0.118	0.547	0.687	0.786	0.867	2.094	0.042
810	0.106	0.501	0.619	0.734	0.856	1.997	0.036

For a more extensive assessment of the PSF at the quadrant center field points, long-exposure, saturated images were combined with unsaturated ones to produce the high dynamic range images shown in Figure 2. The apparent peak pixel signal of each image is approximately 10^7 e⁻, scaled by relative exposure time from the measured signal, ~50 ke⁻. A blocked column in the wings of the 350 nm PSF at UV14 image was corrected by replacement with adjacent pixel averages before analysis. There are several interesting features present in the images, which subtend 16 arcsec square.

Faint flares are visible, especially in the PSFs at 350 and 633 nm, at PA ~20° and 170°. These appear to rotate, in concert with the spider diffraction, as field position changes, so are almost certainly due to glints within the CASTLE stimulus. Also faintly visible, especially in the 350 nm image is a curious set of 18 faint spots arrayed in a ring centered on the UV point source images. The radius is proportional to the wavelength, indicating a diffraction phenomenon, and the position angle does not vary with field location, as do the spider diffraction features, which implicates a source on, or downstream of, the CASTLE steering flats, perhaps within the WFC3 instrument. This ring is at the same

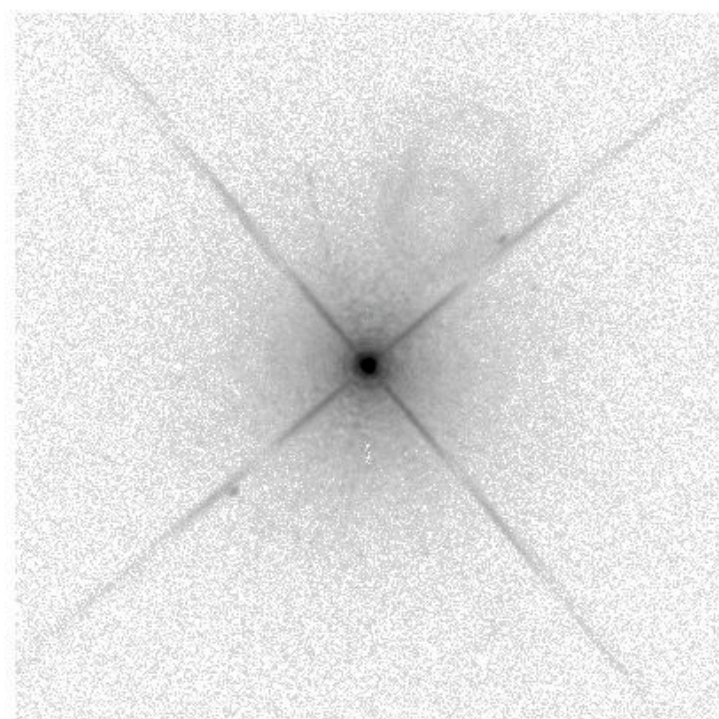
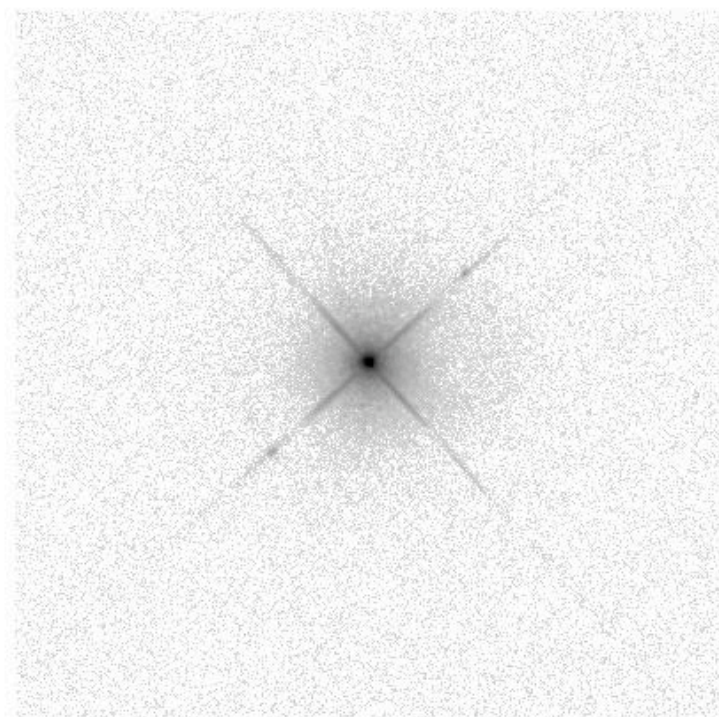


Figure 2. High dynamic range composite images at 250 nm (top, at UV13) and 350 nm (bottom, at UV14) shown on a log stretch from 1 to 10^5 DN, covering 16 arcsec square.

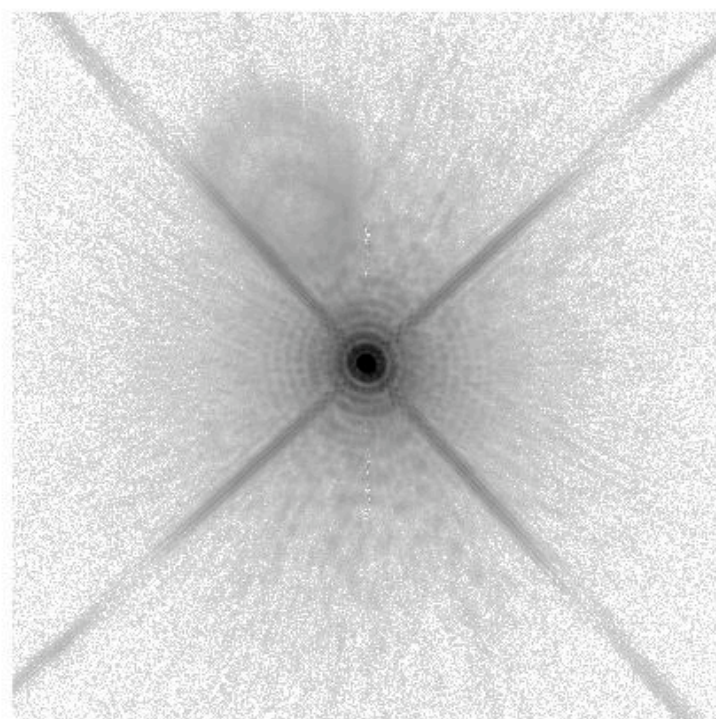
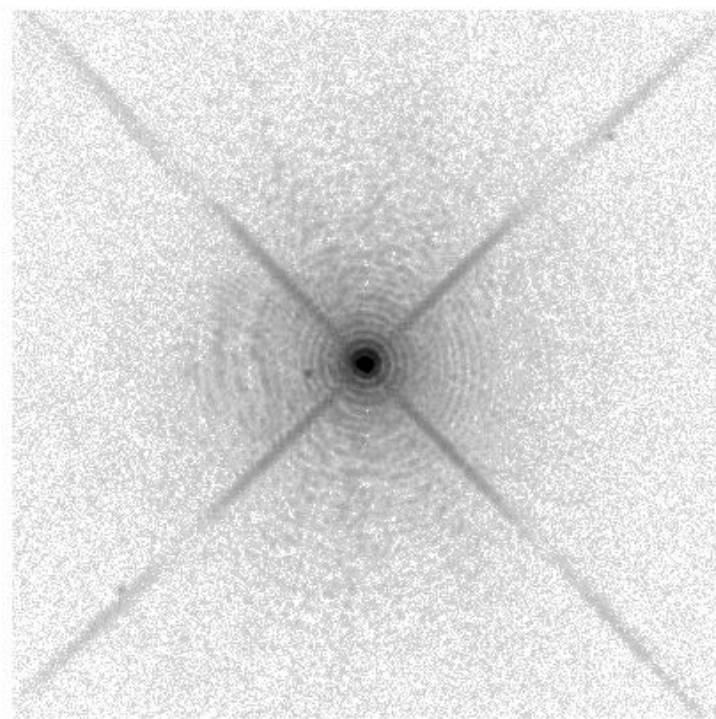


Figure 2 (cont'd.) High dynamic range composite images at 633 nm (top, at UV15) and 810 nm (bottom, at UV16) shown on a log stretch from 1 to 10^5 DN, covering 16 arcsec square.

Table 3. Measured Encircled Energy and Peak Fraction

UV01							
λ (nm)	peak	0.150	0.200	0.250	0.350	FWHM	sharp
250	0.148	0.725	0.826	0.875	0.921	1.860	0.076
350	0.126	0.667	0.785	0.843	0.899	2.082	0.059
633	0.133	0.551	0.692	0.783	0.865	2.005	0.043
810	0.111	0.507	0.624	0.741	0.860	1.950	0.038

UV09							
λ (nm)	peak	0.150	0.200	0.250	0.350	FWHM	sharp
250	0.177	0.717	0.821	0.873	0.917	1.884	0.072
350	0.126	0.673	0.791	0.850	0.906	2.076	0.059
633	0.112	0.550	0.690	0.791	0.870	2.082	0.043
810	0.120	0.512	0.626	0.740	0.858	1.930	0.038

UV02							
λ (nm)	peak	0.150	0.200	0.250	0.350	FWHM	sharp
250	0.170	0.724	0.822	0.871	0.915	1.806	0.075
350	0.136	0.672	0.786	0.841	0.898	2.048	0.059
633	0.111	0.550	0.693	0.794	0.874	2.129	0.042
810	0.110	0.508	0.627	0.742	0.862	1.975	0.037

UV10							
λ (nm)	peak	0.150	0.200	0.250	0.350	FWHM	sharp
250	0.189	0.730	0.836	0.895	0.953	1.807	0.080
350	0.136	0.659	0.771	0.830	0.890	2.033	0.058
633	0.126	0.544	0.683	0.779	0.860	2.149	0.040
810	0.102	0.499	0.617	0.732	0.856	2.015	0.036

UV03							
λ (nm)	peak	0.150	0.200	0.250	0.350	FWHM	sharp
250	0.176	0.736	0.834	0.880	0.921	1.798	0.078
350	0.148	0.694	0.802	0.852	0.905	1.976	0.065
633	0.139	0.561	0.703	0.797	0.873	1.915	0.046
810	0.104	0.513	0.632	0.746	0.866	1.947	0.039

UV11							
λ (nm)	peak	0.150	0.200	0.250	0.350	FWHM	sharp
250	0.141	0.698	0.814	0.874	0.923	1.976	0.067
350	0.135	0.663	0.781	0.842	0.902	2.063	0.058
633	0.125	0.545	0.687	0.784	0.868	2.205	0.040
810	0.101	0.502	0.626	0.737	0.858	1.905	0.038

UV04							
λ (nm)	peak	0.150	0.200	0.250	0.350	FWHM	sharp
250	0.172	0.717	0.819	0.869	0.917	1.843	0.073
350	0.161	0.680	0.790	0.843	0.900	1.963	0.062
633	0.127	0.555	0.700	0.796	0.874	2.051	0.044
810	0.099	0.505	0.625	0.743	0.862	1.958	0.038

UV12							
λ (nm)	peak	0.150	0.200	0.250	0.350	FWHM	sharp
250	0.137	0.669	0.799	0.864	0.918	2.166	0.057
350	0.126	0.632	0.761	0.830	0.896	2.216	0.051
633	0.120	0.539	0.676	0.777	0.861	2.152	0.040
810	0.109	0.496	0.613	0.730	0.854	1.995	0.035

UV05							
λ (nm)	peak	0.150	0.200	0.250	0.350	FWHM	sharp
250	0.160	0.679	0.794	0.853	0.909	1.946	0.063
350	0.146	0.647	0.764	0.827	0.892	2.033	0.055
633	0.122	0.542	0.680	0.782	0.865	2.058	0.042
810	0.101	0.494	0.610	0.725	0.848	2.035	0.035

UV13							
λ (nm)	peak	0.150	0.200	0.250	0.350	FWHM	sharp
250	0.163	0.742	0.838	0.885	0.925	1.785	0.081
350	0.171	0.695	0.800	0.851	0.903	1.891	0.066
633	0.115	0.562	0.700	0.800	0.872	1.993	0.046
810	0.117	0.516	0.632	0.748	0.866	1.911	0.039

UV06							
λ (nm)	peak	0.150	0.200	0.250	0.350	FWHM	sharp
250	0.147	0.673	0.787	0.848	0.904	1.942	0.062
350	0.141	0.636	0.754	0.815	0.880	2.056	0.053
633	0.107	0.540	0.672	0.778	0.858	2.044	0.042
810	0.111	0.498	0.610	0.723	0.850	1.938	0.036

UV14							
λ (nm)	peak	0.150	0.200	0.250	0.350	FWHM	sharp
250	0.151	0.717	0.819	0.870	0.917	1.881	0.071
350	0.131	0.673	0.786	0.842	0.899	2.093	0.059
633	0.120	0.557	0.695	0.795	0.869	2.080	0.043
810	0.116	0.511	0.622	0.745	0.861	1.910	0.038

UV07							
λ (nm)	peak	0.150	0.200	0.250	0.350	FWHM	sharp
250	0.124	0.651	0.785	0.854	0.913	2.191	0.055
350	0.113	0.610	0.742	0.824	0.894	2.324	0.047
633	0.103	0.531	0.673	0.775	0.866	2.211	0.039
810	0.095	0.478	0.598	0.709	0.842	2.354	0.031

UV15							
λ (nm)	peak	0.150	0.200	0.250	0.350	FWHM	sharp
250	0.161	0.705	0.812	0.867	0.916	1.913	0.069
350	0.123	0.651	0.772	0.834	0.894	2.168	0.054
633	0.106	0.545	0.687	0.787	0.870	2.113	0.042
810	0.120	0.508	0.623	0.738	0.858	1.903	0.038

UV08							
λ (nm)	peak	0.150	0.200	0.250	0.350	FWHM	sharp
250	0.128	0.637	0.763	0.830	0.898	2.138	0.053
350	0.128	0.609	0.736	0.805	0.875	2.184	0.048
633	0.103	0.521	0.665	0.763	0.850	2.166	0.038
810	0.092	0.474	0.600	0.711	0.841	2.210	0.031

UV16							
λ (nm)	peak	0.150	0.200	0.250	0.350	FWHM	sharp
250	0.156	0.705	0.811	0.866	0.918	1.871	0.070
350	0.126	0.656	0.772	0.830	0.891	2.091	0.057
633	0.113	0.553	0.693	0.795	0.871	2.146	0.043
810	0.095	0.497	0.616	0.731	0.855	2.008	0.036

radius as the two brighter, diametrically opposed spots, just off the lower-left and upper-right (spacecraft V2 axis) spider features, that exhibit the same behavior; the flux fraction in each of these two spots is $< 0.004\%$. Their origin indeterminate, these features were left uncorrected.

Several ghost features are also present. The set of large diameter “donut” ghosts apparent in the 350 and 810 nm images are due to reflections between the four surfaces of the two detector windows, as expected. A faint, point-like ghost is also produced by the F625W filter, at PA $\sim 95^\circ$ in the image at field point UV15; its total energy fraction is $\sim 0.03\%$.

In order to extrapolate these lab data to expected on-orbit results, we begin with modeling the images using straightforward calculations, including only an independent assessment of the low order WFE (Hartig, 2008b), the CASTLE pupil mask and a reasonable estimate of the detector MTF, due mostly to charge diffusion. The latter is approximated by convolving the PSF with a Gaussian jitter kernel, and may be anchored with an early DCL measurement of the CCD pixel response function (PRF) at 850 nm (Foltz, 2003).

The PRF for backside-illuminated CCDs is expected to be considerably worse at shorter wavelengths, where the carriers are all created near the backside surface where the pixel-defining field is weak, resulting in increased charge diffusion to neighboring pixels. We may attempt to estimate the PRF by comparing model PSFs with the observed short wavelength images. The peak fraction is quite sensitive to the PRF, but, unfortunately, it is also very sensitive to image centration with respect to the pixel boundaries. The EE, even in a relatively small diameter (0.15 arcsec) is fairly insensitive to both charge diffusion and PSF centration. The image width, as assessed by a subsampling Gaussian fit algorithm, and the PSF sharpness are better parameters for this fit, as they are relatively insensitive to centration while retaining significant sensitivity to the PRF. The adopted modeling approach matches the distribution of the ensemble of these parameters with the measured results shown in Tables 2 and 3, by applying varying amounts of “jitter” and offsets from pixel center. Because the longer wavelength images, obtained with short exposure times, are affected by the shutter vibration, we use only the measurements at 250 nm and assume a linear relation of effective PRF “jitter” amplitude with wavelength, the long wavelength value anchored by the DCL measurement. The best empirical fit to the pixel response convolution kernel is shown in Table 4. As in earlier studies, these results indicate that the CEI specification requiring that 90% of the energy from a small spot lie within the central pixel is not met. These kernels are similar to those found by Krist (2004) for the backside-illuminated CCDs with the same pixel dimensions in the ACS/WFC.

Table 4. CCD Pixel Response Functions

250 nm			850 nm		
0.022	0.104	0.022	0.006	0.064	0.006
0.104	0.496	0.104	0.064	0.720	0.064
0.022	0.104	0.022	0.006	0.064	0.006

For each of the composite images shown in Fig 2 we have computed the EE and azimuthally-averaged (AA) PSF, normalized to 1 at the peak, for comparison with the CASTLE+WFC3 model. These are shown in Figure 3, which plots the measured EE (left panel) and AA PSF intensity (right panel) as solid lines, with the CASTLE+WFC3 model shown as dotted lines. The agreement between measurement and model is very good, from radii of 40 mas (1px) to 5 arcsec. The differences in modulation of the AA PSF wings beyond 1 arcsec are at least partially due to inaccuracies in the model related to the diffraction of the spiders.

Because the EE specification applies to the WFC3 installed in the HST, the ground-based measurements must be extrapolated with the aid of model computations that account for differences between the CASTLE and HST to predict on-orbit performance. These differences include the smaller central obscuration of the OTA, its PM mounting pads, and the mid-spatial-frequency zonal polishing errors of its mirrors. The EE specifications in the PSF wings (for 250 nm and 633 nm) are shown in Figure 3 as diamonds. If taken at face value, the plots indicate that the camera readily meets its requirements. Actual on-orbit performance, including the HST telescope properties, is approximated by the dashed OTA+WFC3 model curves, which show the effects of the OTA mid-frequency WFE on the near wings. While the projected EE at 633 nm (83% in 0.25 arcsec) exceeds the specified goal, the 250 nm EE in 0.2 arcsec diameter is expected to just meet the requirement (70%), which was recently modified to reflect the known OTA performance contribution.

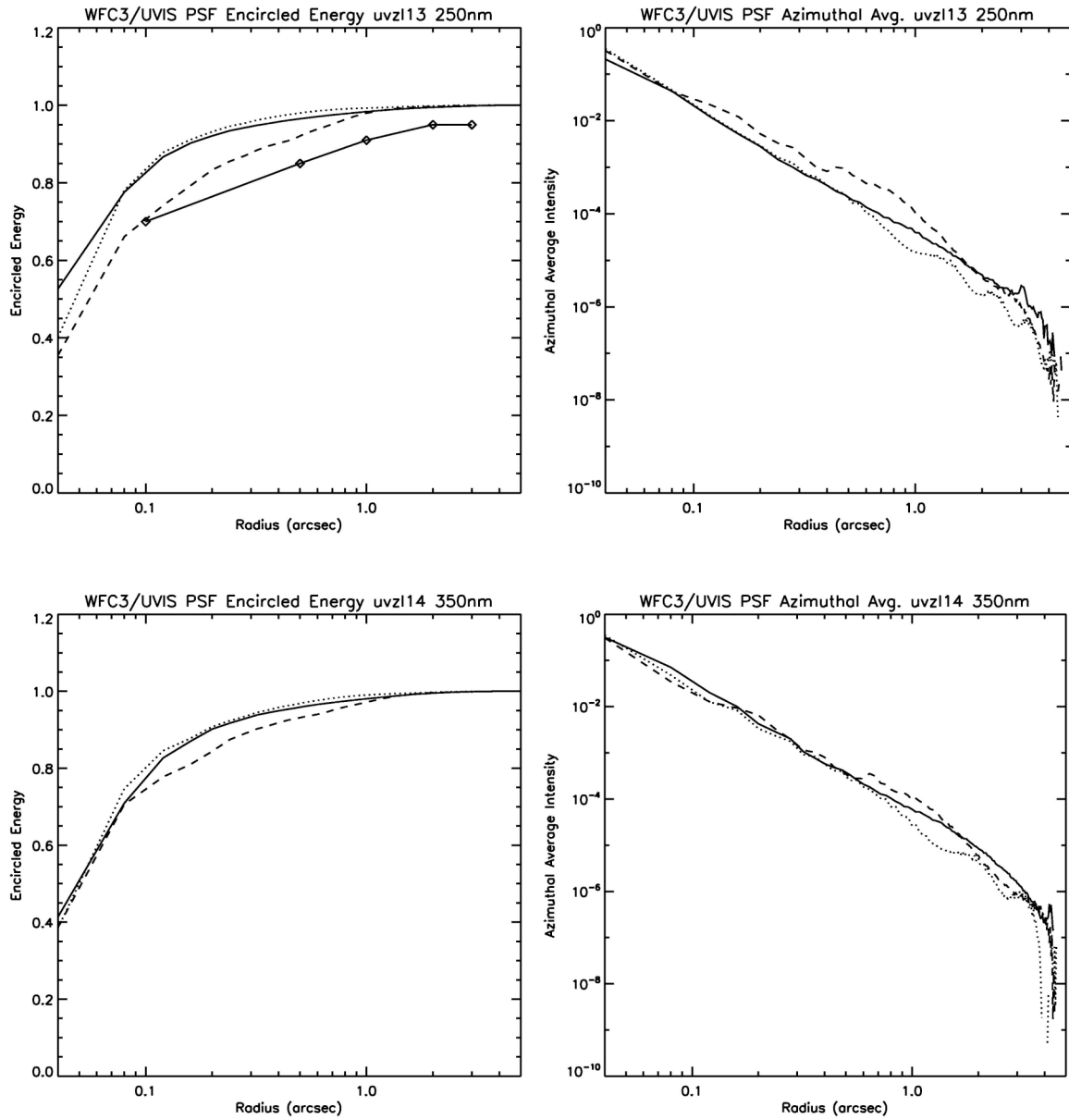


Figure 3. Comparison of composite measured (solid line), CASTLE model (dotted line), and OTA model (dashed line) images at field points UV13 and UV14 at 250, and 350 nm, respectively. The left frames show the encircled energy, from radii of 1 px to 5 arcsec, and the right frames plot the azimuthally-averaged PSF. The EE specifications (at 250 nm) are shown as diamonds.

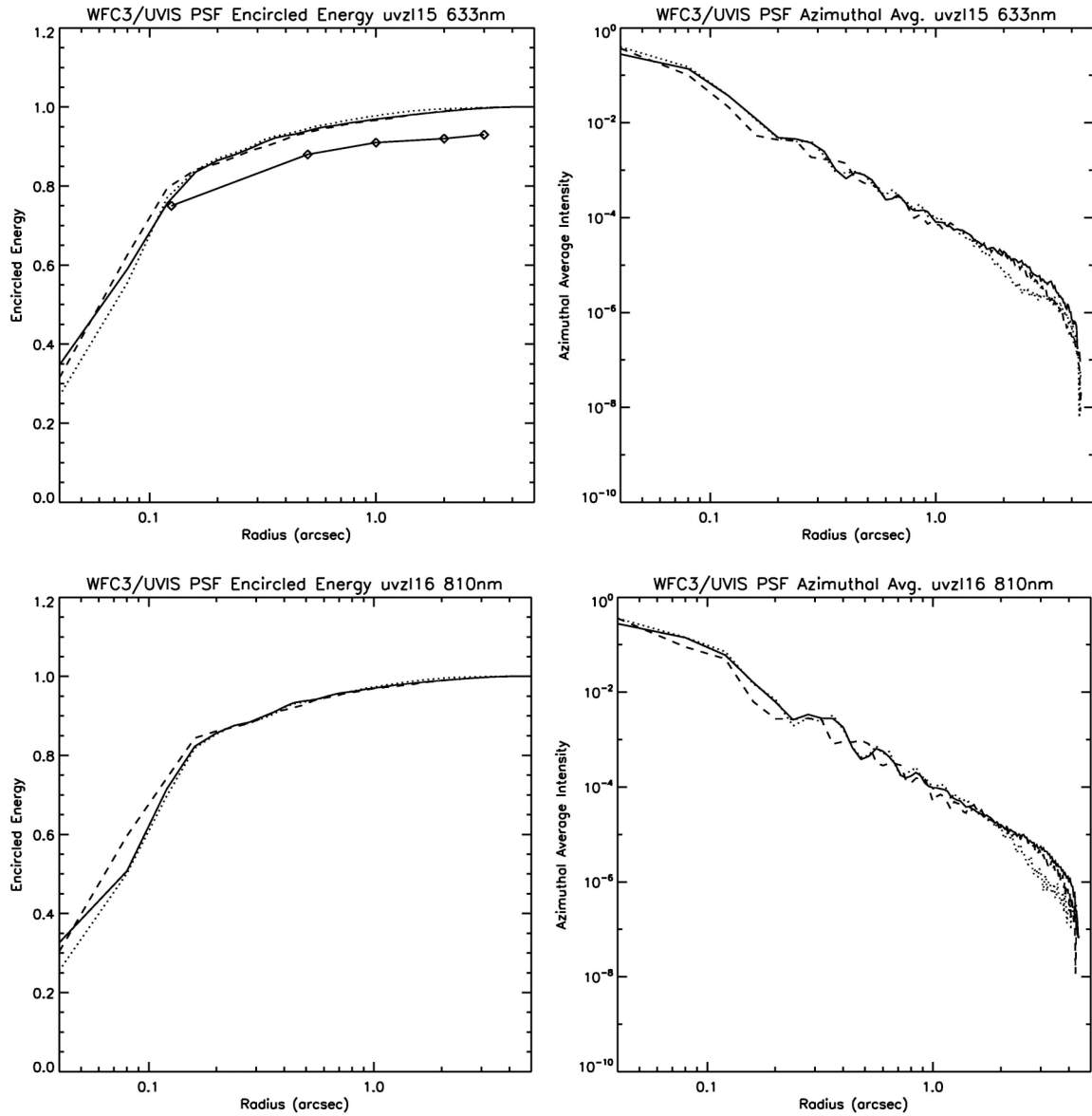


Figure 3 (cont'd.) Comparison of composite measured (solid line), CASTLE model (dotted line), and OTA model (dashed line) images at field points UV15 and UV16 at 633 and 810 nm, respectively. The left frames show the encircled energy, from radii of 1 px to 5 arcsec, and the right frames plot the azimuthally-averaged PSF. The EE specifications (at 633 nm) are shown as diamonds.

Conclusion

We conclude that the flight configuration WFC3 UVIS optical performance is generally excellent. Aside from faint filter ghosts, such as those apparent in the F336W and F814W images (see Brown 2008, for a complete discussion) and a very faint symmetrical pair of weak straylight features the origin of which is not yet understood, the UVIS channel is performing as expected over the field. Our modeling indicates that the UVIS channel will readily meet its on-orbit image quality (EE) specifications at 633 nm; the (amended) requirements at 250 nm, more difficult due to the effects of the OTA mid-frequency WFE, will also likely be achieved.

References

Brown, T. "UVIS Channel Filter Ghosts After Filter Replacement", STScI ISR WFC3-2007-09, 2007.

Foltz, R. "Single Pixel Illumination Report", GSFC DCL Internal Report, 2004.

Hartig, G.F. and Baggett, S. "Preliminary WFC3 UVIS PSF Evaluation", STScI ISR WFC3-2004-08, 2004.

Hartig, G.F. "WFC3 UVIS PSF Evaluation in Thermal-Vacuum Test #3", STScI ISR WFC3-2005-10, 2005.

Hartig, G.F. "WFC3 Optical Alignment Characterization in Thermal-Vacuum Test #3", STScI ISR WFC3-2008-32, 2008a.

Hartig, G.F. "WFC3 Optical Wavefront Error Characterization in Thermal-Vacuum Test #3", STScI ISR WFC3-2008-31, 2008b.

Krist, J.E. "Position-dependent CCD Charge Diffusion: Results from HST/ACS", SPIE 5499, 328, 2004.